

## Evaluation and Characterization of Reduced Graphene Oxide Nanosheets as Anode Materials for Lithium-Ion Batteries

Changjing Fu<sup>\*</sup>, Guogang Zhao<sup>\*</sup>, Haijun Zhang, Shuang Li

Engineering Research Academy of Graphite New Materials, Heilongjiang Institute of Science & Technology, 1 Tangchang Avenue, Harbin 150027, PR China

<sup>\*</sup>E-mail: [fcj\\_hit@163.com](mailto:fcj_hit@163.com), [zgg1963@126.com](mailto:zgg1963@126.com)

Received: 25 March 2013 / Accepted: 16 April 2013 / Published: 1 May 2013

---

High quality reduced graphene oxide (rGO) nanosheets were prepared from natural graphite through oxidation followed by solvothermal reduction method. The morphology, structure and composition of graphene oxide (GO) and rGO were characterized by scanning electron microscope (SEM), transmission electron microscope (TEM), Raman spectrum, X-ray diffraction (XRD), and X-ray photoelectron spectroscopy (XPS). The electrochemical performances of rGO nanosheets as anode materials for lithium-ion batteries were evaluated in coin-type cells versus metallic lithium. Results showed that the obtained rGO exhibited a higher reversible specific capacity of 561 mAh g<sup>-1</sup> at a current density of 100 mA g<sup>-1</sup> and 166 mAh g<sup>-1</sup> at a current density of 4000 mA g<sup>-1</sup>. The excellent cycling stability and high-rate capability of rGO as anodes of lithium-ion battery were attributed to its few layers structure, large-size sheet, and fast transport kinetics of Li-ion and electron on the interface of electrolyte/electrode.

---

**Keywords:** Lithium-ion battery, Graphene oxide, Microstructure, Electrochemical performance, Reaction Kinetics

### 1. INTRODUCTION

Developing devices and related materials for producing and storing electricity is a key issue to meet the increasing energy demand [1]. Modern electronic devices such as cell phones, laptop computers and electric vehicles require high-performance batteries to power them [2]. Lithium-ion battery (LIB), as an effective electrochemical energy storage device, has attracted much interest recently. Great efforts have been devoted to develop different types of materials with high reversible capacity, long cycle life and low cost [3-5]. In 1983, research and development on lithium batteries achieved a breakthrough when a pure lithium metal anode was substituted by a graphitic carbon

material in which lithium was reversibly intercalated and deintercalated [6]. The lamellar structure of graphite inhibited the formation of lithium dendrites and improved thermal stability, the two major problems associated with lithium metal anode. LIB was successfully commercialized as a secondary, rechargeable battery in 1991 [7]. In graphitic carbons, lithium can form intercalation compounds with a stoichiometry of  $\text{LiC}_6$ , giving LIBs a maximum theoretical capacity of  $372 \text{ mAh g}^{-1}$ . Ongoing research efforts have focused on utilizing various carbonaceous nanomaterials to improve this moderate battery capacity as well as cycle life and charge-discharge rates [8]. Especially in recent years, with the development of electronic vehicles, rechargeable LIBs, as attractive power sources, have been receiving worldwide attention in scientific and industrial fields. Therefore, developing advanced electrode materials with less resistance and higher rate capability seems to be of great importance [9].

The main reason for the lower rate capability of LIBs is the polarization of electrochemical processes on electrodes [10], including electrochemical reactions on interfaces of active materials and electrolytes, lithium diffusion in active materials, lithium-ion transportation through electrolyte and electron transfer through active materials. The polarization would be decreased by using nanocomposite electrodes of active materials and electronic conductive materials, such as carbon [11]. Nanostructure electrode materials are powerful candidates for achieving fast electrode reactions rates, and delivering high power in rechargeable LIBs [12-16].

Graphene, a two-dimensional (2-D) nanostructure of carbon, has attracted a great deal of attention, though it was experimentally discovered in 2004 [17]. Its special structure of monolayer graphite endows it with many excellent properties such as good chemical stability, high quantum hall effect, and extraordinary electronic transport properties [18, 19]. Besides, Graphene as an alternative form of conductive carbon also provides it as a perfect substrate to host active nanomaterials for energy applications [20].

In recent years, graphene has been produced by many kinds of physical and chemical methods. Among them, graphene derived from chemical oxidation-reduction method exhibits extensive defects, while graphene prepared by CVD, liquid phase production, and mechanical cleavage of graphite presents no defects. Graphene oxide (GO) has been widely used as starting materials for the synthesis of processible graphene, and the modified hummers method is very fruitful for the synthesis of GO [21, 22]. The surfaces of GO sheets prepared by this method are highly oxygenated, bearing hydroxyl, epoxide, diol, ketone and carboxyl functional groups that could alter the van der waals interactions significantly and leads to a range of solubility of it in water and oxygenic solvents [23, 24]. GO is most commonly reduced by chemical and thermal treatments in order to remove the oxygen-containing functional groups [25]. These treatments could not form graphene but produce another nonstoichiometric partially reduced GO (rGO) which remains disordered. The heterogeneous surfaces of rGO consisting of edge plane nano bands are exclusively the sites of electro-catalysis, whereas the basal plane islands are electro-chemically inert [26]. According to the report from Robinson and his coworkers [27], 1% defect density is estimated to result in a  $10^3$  factor increase in the heterogeneous electron transfer rate constant. Hence, the preparation method of graphene has a dramatic influence on the materials properties and electrochemical reactivity.

In this article, we presented rGO nanosheets prepared through the modified Hummers method combined with solvothermal reduction method as the anode active materials of LIBs. The structure and electrochemical properties of rGO nanosheets were characterized and analyzed in detail. The controlling factors inhibiting the reaction kinetics of rGO anode process were revealed.

## 2. EXPERIMENTAL

### 2.1 Synthesis of rGO

GO was synthesized from natural graphite by the modified hummers method [22]. In this reaction, graphite (2 g, 1 wt. equiv.),  $\text{NaNO}_3$  (1 g, 0.5 wt. equiv.), and concentrated  $\text{H}_2\text{SO}_4$  (100 mL) was first stirred together in an ice bath for 30 min. The temperature of the mixture was controlled at approximately 1 °C. Next,  $\text{KMnO}_4$  (8 g, 4 wt. equiv.) was slowly added in portions to keep the reaction temperature below 10 °C. The mixture was then transferred to a 35 °C water bath and stirred for 3 h, at which time it became thickened and the volume increased more than one time of its original volume. Water (200 mL) was added subsequently to produce a large exotherm to 98 °C. External heating was introduced to maintain the reaction temperature at 98 °C for 1 h. The mixture gradually became brown. After that, warm water (400 mL) was added to produce another exotherm, followed by the slow addition of 30 ml  $\text{H}_2\text{O}_2$  (30%) to reduce residual permanganate and manganese dioxide to colorless soluble manganese sulfate. The color of the mixture turned gradually from dark brown to bright yellow. Then, the warm solution was centrifuged and washed with HCl (5 wt.%) and water. It was repeated until the pH value of the filtrate was close to 7 and no deposit appeared in the filtrate with  $\text{BaCl}_2$  test.

Thus-prepared filtrate was dried in a vacuum oven at 60 °C for 2 days to obtain graphite oxide. The filter cake was re-dispersed in ethanol with mechanical agitation or sonication using an ultrasonic cell disruptor, giving a solution of exfoliated GO. Subsequently, GO solution was put into an autoclave and heated to 160 °C for 4 h to reduce GO to rGO. The as-synthesized product was isolated by centrifugation, washed with water and ethanol, respectively, and finally dried in a vacuum oven at 60 °C for 24 h.

### 2.2. Characterization of GO and rGO nanosheets

As-prepared materials were characterized by means of X-ray diffraction (XRD, Rigaku MinFlex, D/max 2550-PC) with Cu Ka radiation ( $\lambda=0.15406$  nm). The data was collected between scattering angles ( $2\theta$ ) of 10-90° at a scanning rate of 2°  $\text{min}^{-1}$ . The microstructure of GO and rGO samples were observed by transmission electron microscopy (TEM, JEOL-2100F) and scanning electron microscopy (SEM, JEOL-5600LV). TEM specimens were prepared by drop-casting the as-prepared sample dispersions onto carbon-coated TEM grids and dried in air. X-ray photoelectron spectroscopy (XPS) data were taken on an AXIS Ultra instrument from Kratos Analytical in the range of 1-1300 eV to investigate the surface chemistries of the obtained materials. Raman spectra were

obtained with a WITec CRM200 confocal Raman microscopy system (Labram-HR, France) with a laser wavelength of 514.5 nm and a spot size of 2  $\mu\text{m}$ . The Si peak at 520  $\text{cm}^{-1}$  was used as a reference to calibrate the wavenumber.

### 2.3. Electrochemical testing of rGO nanosheets in lithium-ion batteries

To evaluate the electrochemical performance, composite electrodes were constructed by mixing the active materials, conductive carbon black, and polyvinylidene fluoride (PVDF), in a weight ratio of 70:20:10. The mixture was prepared as slurry in N-methyl pyrrolidinone (NMP) and spread onto copper foil by using the doctor-blade technique. The electrode was dried under vacuum at 120  $^{\circ}\text{C}$  for 12 h. Cells were assembled inside an argon-filled glovebox by using a lithium-metal foil as the counter electrode and the reference electrode and the microporous polypropylene as the separator. The electrolyte used was 1 M  $\text{LiPF}_6$  in a 1:1 weight ratio ethylene carbonate (EC): dimethyl carbonate (DMC) solvent. Assembled cells were allowed to soak overnight before electrochemical testing. Electrochemical impedance spectroscopy (EIS) measurements were carried out in a two-electrode cell in the frequency range from 0.1 Hz to 100 kHz on a Princeton electrochemical workstation (M2273). Galvanostatic charge and discharge of the assembled cells were performed with a NEWARE battery tester at a voltage window of 0.01 and 3.0 V (vs.  $\text{Li}^+/\text{Li}$ ). Cyclic Voltammetry (0.01-3 V, 0.2  $\text{mV s}^{-1}$ ) was performed with an electrochemical workstation (CHI660C). All the tests were conducted at room temperature ( $25 \pm 1$   $^{\circ}\text{C}$ ).

## 3. RESULTS AND DISCUSSIONS

### 3.1 Morphology and structure of GO and rGO nanosheets

The morphology and structure of GO and rGO nanosheets were investigated through SEM and TEM observation. Figure 1a presents the representative SEM image of free-standing GO nanosheets, revealing a crumpled and rippled structure which was the result of deformation upon the exfoliation and restacking processes. While according to fig. 1c, through TEM observation, independent GO nanosheets were observed. These single- or few-layer GO nanosheets were larger than 1.5  $\mu\text{m}$  in wideness and flat, which were due to the sonication in the process of preparing TEM samples destroyed the van der Waals interactions between GO layers, and the existence of a large amount of oxygen-containing functional groups on the surface of GO nanosheets. The rGO nanosheets, however, are layer structured, irregular and folding, as shown in the SEM image of fig.1b. They are entangled with each other. Figure 1d showed that the single- or few-layer rGO nanosheets were with lots of wrinkles. Corrugation and scrolling suggested the intrinsic nature of graphene, because the 2D membrane structure would be thermodynamically stable *via* blending [28]. Above all, this kind of special microstructure of rGO could provide more spaces for lithium ion storage.

XRD patterns of GO and rGO nanosheets are presented in Fig.2. The characteristic peak (002) of graphite at 26.58 $^{\circ}$  disappeared after oxidation, while an additional peak at 11.42 $^{\circ}$  was observed,

which was corresponding to the (001) diffraction peak of GO. Not only that, but the d-spacing of GO was 1.31 folds larger than that of graphite, increased to 0.774 nm.

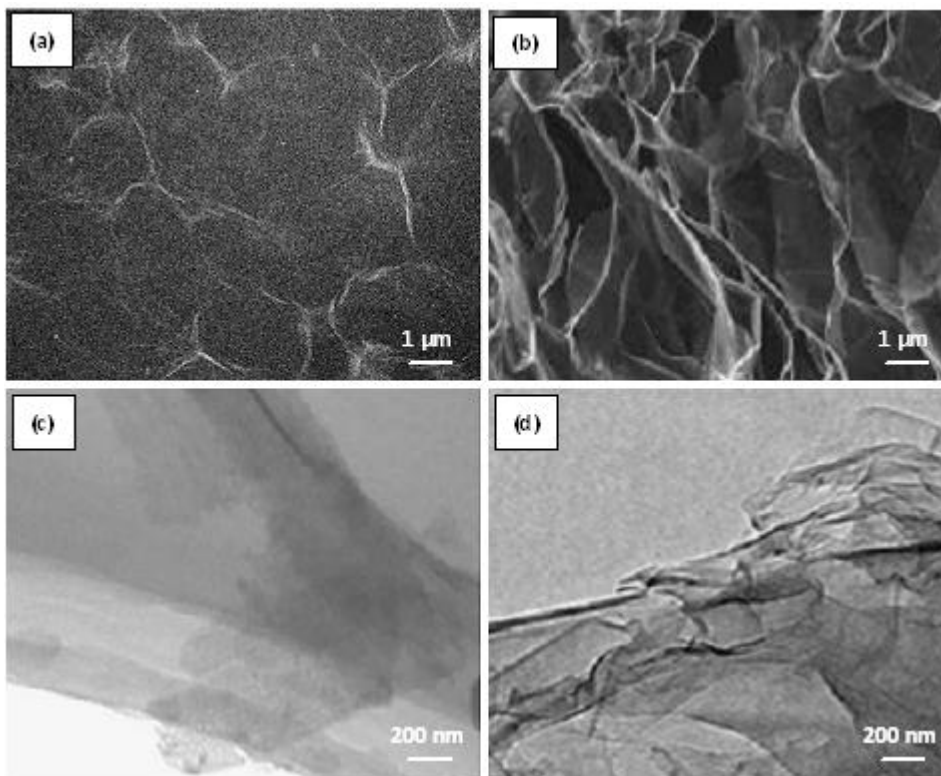


**Figure 1.** Microstructure observation of GO and rGO: (a) SEM image of GO, (b) SEM image of rGO, (c) TEM image of GO and (d) TEM image of rGO .

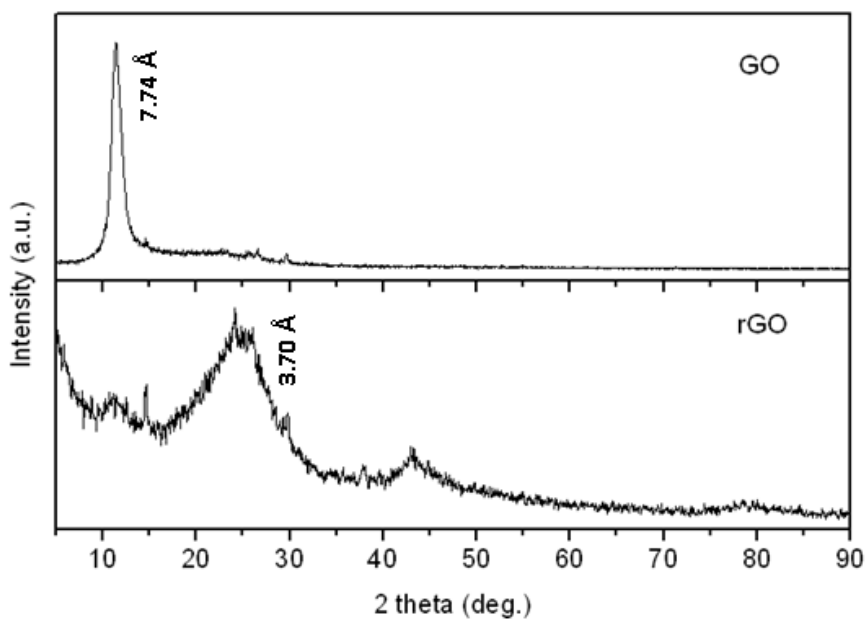


**Figure 2.** XRD patterns of GO and rGO nanosheets.

The larger interlayer distance of GO might be due to the formation of oxygen-containing functional groups, such as hydroxyl, epoxy and carboxyl [29]. Thus, from the XRD pattern of GO, it could be inferred that the original graphite powders had almost been completely oxidized. However, the oxygen-containing functional groups of GO couldn't be completely got rid of through solvothermal reduction. A small characteristic diffraction peak of graphite oxide (001) at approximately  $14^\circ$  still remained in the XRD pattern of rGO, besides a broad diffraction peak (002) of graphite at about  $24^\circ$ . The broadening and shift of the characteristic diffraction peak of graphite from  $26.58^\circ$  to  $24^\circ$  was due to the short-range order in stacked stacks. The interlayer spacing of rGO was 0.37 nm, slightly larger than that of graphite, which was resulted from the small amount of residual oxygen-containing functional groups or other structural defects [30].

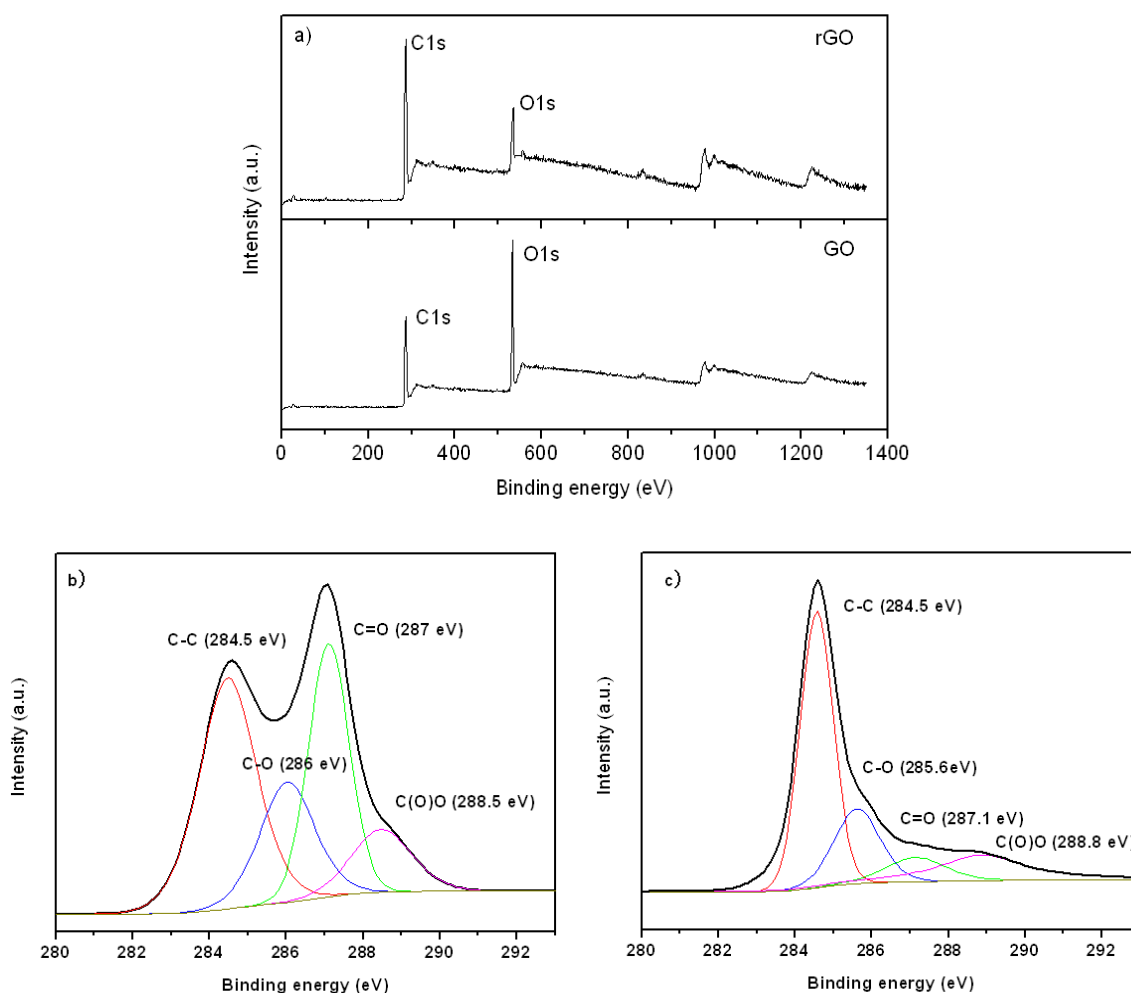


**Figure 3.** Raman spectra (D and G bands) of GO and rGO nanosheets.

The peak areas calculation of C and O elements from XPS spectra survey scan in fig.3a revealed that the ratio of C and O atomic element increased from 2.7 in GO to 10.3 in rGO and about 13 at.% of oxygen was retained in rGO. These results further confirmed the insufficient reduction of GO by solvothermal reduction method, which was consistent with results of XRD, although a

characteristic peak of aromatic or conjugated systems, around 290.8 eV, resumed after the reaction (Fig.3a). The  $C_{1s}$  spectra of six selected products in GO and rGO are presented in fig. 3b and c, respectively. Differences between the  $C_{1s}$  spectra of GO and rGO are evident in shape and peak identity. XPS analysis demonstrated that a significantly larger proportion of oxygen in GO existed in the form of C=O functionalities and fewer proportion of oxygen were associated with hydroxyl and COOH groups (fig.3b). However, according to  $C_{1s}$  spectra analysis of rGO in fig.3c, after the solvothermal reduction of GO, the peaks of oxygen-containing groups at 284.5 eV (C-O), 286.8 eV (C=O), and 289 eV (O-C=O) decreased to a different degree. The proportion of C=O and COOH groups decreased greatly, while the proportion of hydroxyl groups changed slightly, demonstrating that solvothermal reduction method have little effect on the deoxygenation of hydroxyl groups, although most of the other oxygen-containing functional groups were removed.

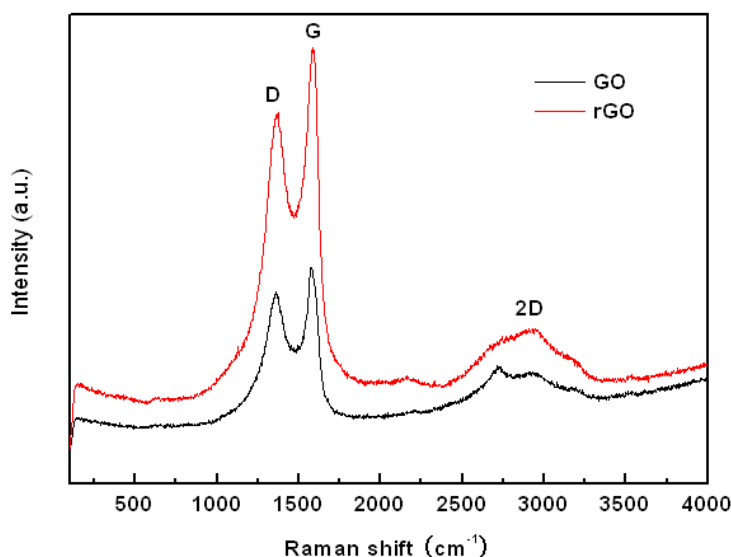


**Figure 4.** XPS spectra of GO and rGO nanosheets (a),  $C_{1s}$  spectra of GO (b) and  $C_{1s}$  spectra of rGO (c).

Significant structural changes occurring during the chemical processing from GO to rGO nanosheets have also been characterized by Raman spectroscopy, as shown in Fig.4. In the Raman spectrum of GO, both D band and G band were broadened and shifted to  $1360\text{ cm}^{-1}$  and  $1578\text{ cm}^{-1}$ , respectively. While the D band and G band of the Raman spectrum of rGO appeared at  $1360\text{ cm}^{-1}$  and  $1585\text{ cm}^{-1}$ , respectively. As we all known, D band response originating from the edges can be attributed to either defects or to the breakdown of translational symmetry, while G band is corresponding to the first-order scattering of the  $E_{2g}$  mode of  $sp^2$  domain of graphite. Moreover, the relative strength of D band compared to G band depends strongly on the amount of disorder in the graphitic materials [31]. In this case, the D/G intensity ratio of rGO ( $I_D/I_G$ ) was 1.15, slightly smaller than that of GO ( $I_D/I_G=1.37$ ). Thus, it could be deduced that the extensive oxidation and solvothermal

reduction had induced a certain amount of the decrease in the size of in-plane  $sp^2$  domains, an increase of the edge planes, as well as the expansion of the disorder in the prepared rGO [32].

### 3.2 Electrochemical characteristics of rGO nanosheets

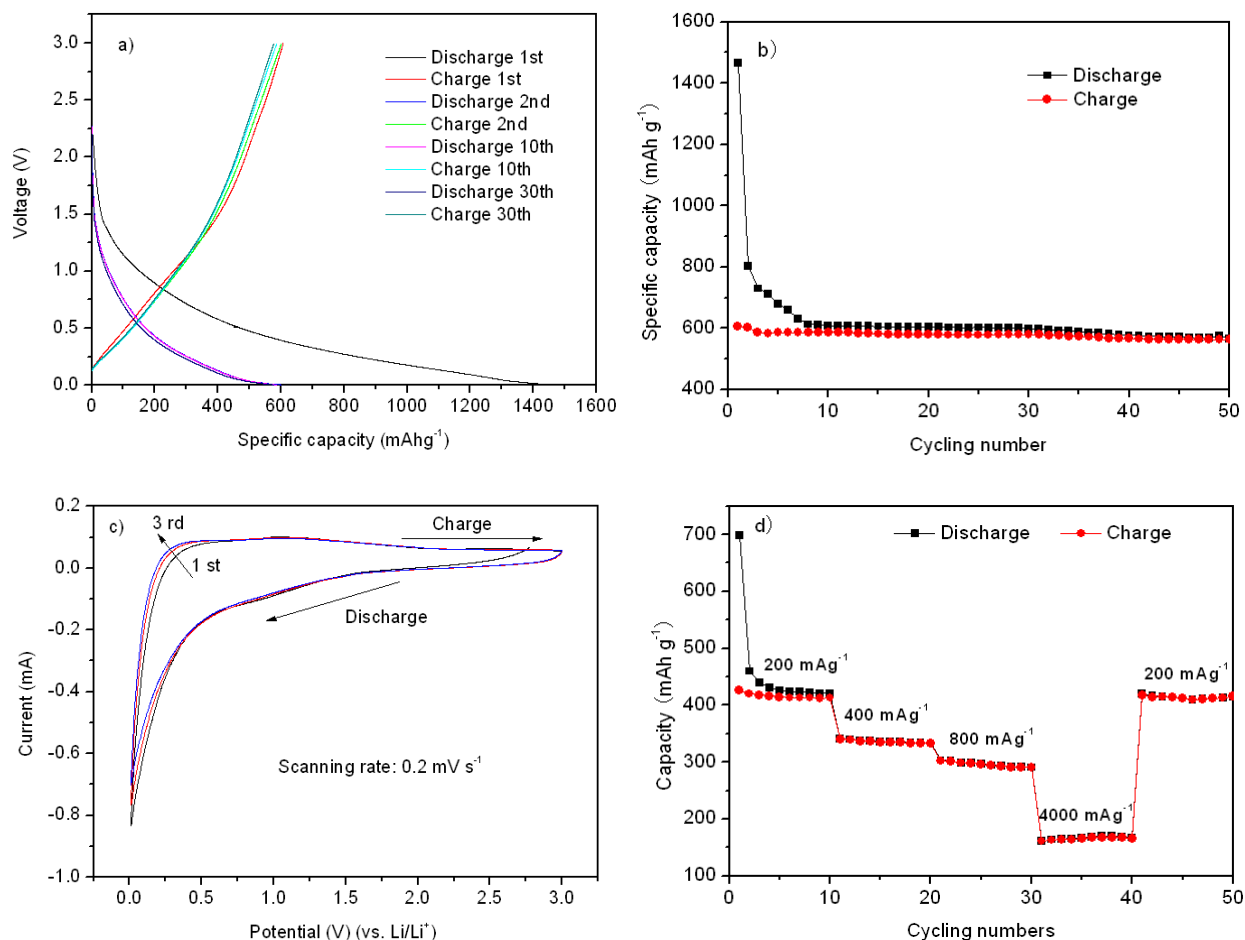


**Figure 5.** Discharge/charge profiles of rGO nanosheets at a current density of  $100 \text{ mAh g}^{-1}$  (a), Capacities versus cycle number between 0.01 and 3 V at a current density of  $100 \text{ mAh g}^{-1}$  (b), Cyclic voltammograms (CV) of rGO nanosheets at a scanning rate of  $0.2 \text{ mV s}^{-1}$  (c) and (d) Cycling performance of rGO nanosheets at various current densities.

The evaluation of electrochemical properties of rGO nanosheets as Li-ion battery anode was performed in a two-electrode cell. Figure 5a presents the first, second and the 30th charge and discharge profiles of rGO electrode between 0.01 and 3.0 V vs.  $\text{Li}^+/\text{Li}$  at a current density of  $100 \text{ mA g}^{-1}$ . They revealed the typical discharge/charge characteristics of graphene nanosheets, such as a large discharge/charge voltage hysteresis, high irreversible capacity and without distinguishable plateaus [33]. The first discharge and charge capacities of rGO electrode were  $1465$  and  $605 \text{ mAh g}^{-1}$ , respectively. The large irreversible capacity of rGO electrode in the first cycle could be attributed to the electrolyte decomposition and formation of solid electrolyte interphase (SEI) layer, both of which took place simultaneously at the rGO nanosheet surface [34]. After the second cycle, the

discharge/charge curves tended to be stable demonstrating the formation of stable SEI film during the first discharge process. The cycle stability of rGO electrode is shown in figure 5b. The reversible specific capacity maintained at 578 and 561 mAh g<sup>-1</sup> after the 30th and 50th cycle, respectively, that was approximately 92.7% retention of the reversible capacity, indicating that solvothermally reduced GO exhibited stable charge/discharge cycling performance. The reason might be due to that the content of hydroxyl groups was relatively larger for rGO prepared by solvothermal reduction method, as shown in fig.3c, which led to the possible reversible reaction of Li with the residual H from hydroxyl groups. The faradic contribution was also favorable to the large reversible capacity, besides the larger surface area and curled morphology of graphene [35].

The cyclic voltammograms (CV) of rGO are shown in figure 5c. The shape of CV curves matched very well with the discharge and charge profiles. The peak close to 0 V resulted from Li<sup>+</sup> intercalation into the carbon based anode. There was no obvious difference between the second and the third cycles, further confirmed the good reversibility of this kind of rGO anode. In addition to the high reversible capacity and exceptional cycle stability, rGO also demonstrated excellent cyclic performance at stepwise current densities. Cycle performance of rGO electrode at different current densities of 200 mA g<sup>-1</sup>, 400 mA g<sup>-1</sup>, 800 mA g<sup>-1</sup> and 4000 mA g<sup>-1</sup> are shown in fig.5d. The reversible capacity was stable at 415 mAh g<sup>-1</sup> after 10 cycles at a current density of 200 mA g<sup>-1</sup>. With the increase of the discharge/charge current density to 400, 800 and 4000 mA g<sup>-1</sup>, respectively, the reversible capacity maintained at 342, 307, 166 mAh g<sup>-1</sup>, respectively, which was remarkably higher than that of the conventional graphite electrode. Moreover, these reversible capacities are comparable to the high quality graphene sheets reported by Lian et al [34]. In their work, GO was reduced by the rapid thermal expansion in nitrogen atmosphere.

EIS testing results are shown in fig.6 to further understand the reason for the improved electrochemical lithium storage performance of rGO. Figure 6a presented the Nyquist plots of rGO carried out at 100 mA g<sup>-1</sup>. The semicircle diameter of rGO decreased 72.3% after the first cycle, revealing the smaller surface film resistance and lithium-ion charge transfer resistance. After 50 cycles, the diameter of the semicircle was still 60% lower than that of rGO without undergoing discharge/charge cycles. This was attributed to the presence of oxygen-containing functional groups at the unorganized carbon sites which resulted in the more irreversible lithium ion inserting in the electrode with the increase of cycle number, and the increase of the electric conductivity of the electrodes [36]. The impedance diagrams were fitted according to the electrical equivalent circuits in fig.6b. The high frequency semicircle is due to the formation of SEI film and the contact resistance, the semicircle in the medium frequency is associated with the charge-transfer impedance on the interface of electrode and electrolyte, while the inclined line at an approximate 45° angle to the real axis corresponds to the lithium-diffusion process within rGO electrodes [37].  $R_e$  is the electrolyte resistance,  $C_{sei}$  and  $R_{sei}$  are the capacitance and resistance of the SEI film, respectively.  $C_{dl}$  and  $R_{ct}$  are the double-layer capacitance and charge-transfer resistance, respectively.  $W$  is the Warburg impedance related to the diffusion of lithium ions into the electrodes.

The values of  $R_e$ ,  $R_{sei}$  and  $R_{ct}$  from EIS fitting results of the electrodes after 50 cycles at different current densities are shown in fig.6c. It can be seen that  $R_e$  and  $R_{sei}$  changed slightly with the increase of current density from 74 mA g<sup>-1</sup>@0.1 C (1C =744 mA g<sup>-1</sup>) to 3720 mA g<sup>-1</sup>@5 C, while  $R_{ct}$

decreased 45% with the increase of current density, from 14.39 Ω at 0.1 C decreased to 7.9 Ω at 5 C, suggesting the enhanced kinetics of Li<sup>+</sup> and electronic transport in rGO anode at higher current densities.

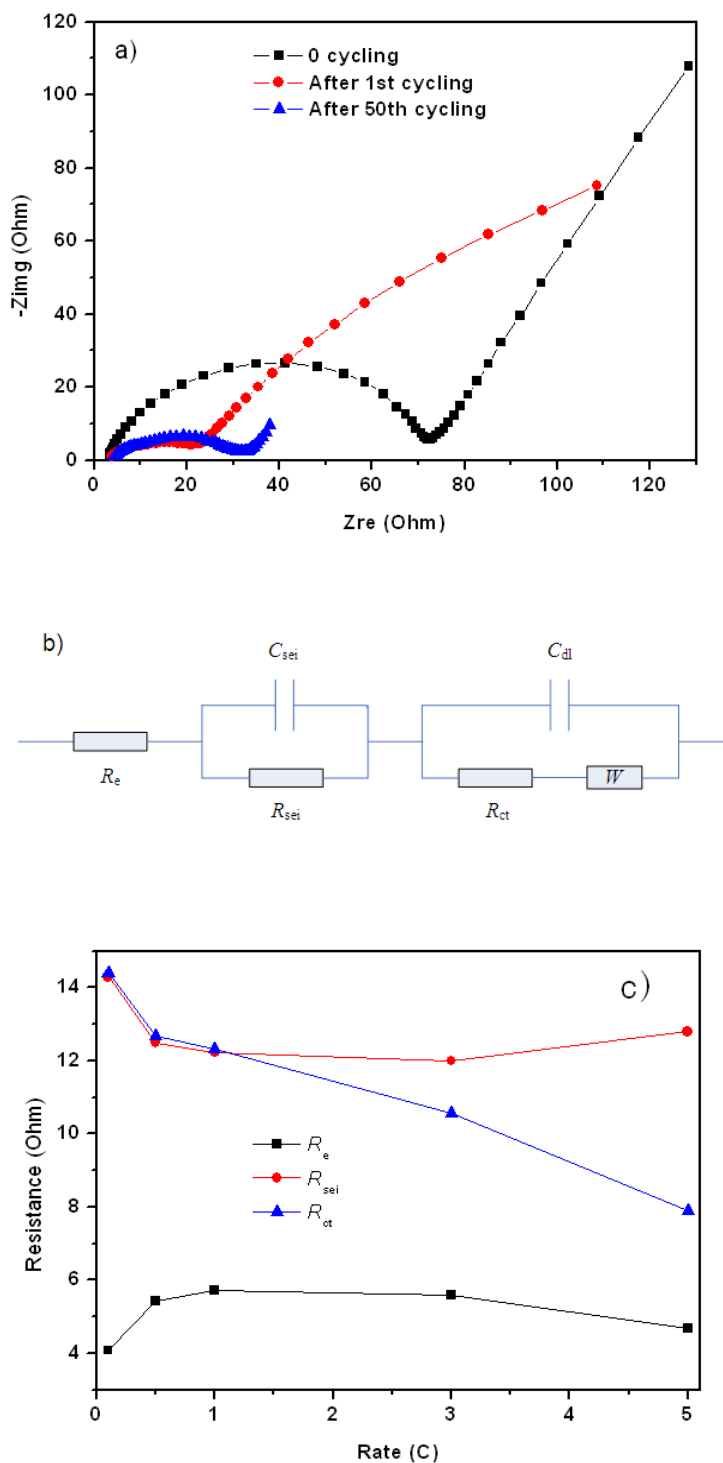


**Figure 6.** Nyquist plot of AC impedance spectra for rGO nanosheets (a), Equivalent electrical circuit used to model (b) and (c) Variations of R<sub>e</sub>, R<sub>sei</sub> and R<sub>ct</sub> as a function of discharge/charge rate of rGO sheets, R<sub>e</sub>, R<sub>sei</sub> and R<sub>ct</sub> were derived using the equivalent circuit (b) for rGO electrodes.

However,  $R_{\text{sei}}$ , occupying more than 40% of the total electrodes resistances at each current density, led to a sluggish transport of  $\text{Li}^+$  and electron. The influence of  $R_{\text{sei}}$  on the electrode performance seemed to be even more prominent at a higher current density, which was resulted from the huge amounts of electrolyte decomposition and the thicker SEI film formation. For example, at a current density of  $3720 \text{ mA g}^{-1}$ ,  $R_{\text{sei}}$  had occupied more than half of the total electrode resistance. Therefore, it can be concluded from the impedance analysis that the electrochemical performance of rGO electrode at a higher current density was retarded primarily due to the slow interface reaction kinetics between the electrolyte/electrode interfaces.

#### 4. CONCLUSIONS

In this article, rGO were prepared by the improved Hummers method combined with solvothermal reduction. RGO prepared by this method exhibited good cycle performance, excellent high-rate discharge/charge properties and better reversible capacity, which was due to the short Li-ion diffusion paths, fast electrochemical reaction kinetics, and more spaces for Li-ion storage. The SEI film resistance caused by the relatively large amount of oxygen-containing functional groups on the rGO surface resulted in the reduced electrode performance at a higher current density. Therefore, further control of the preparation process of rGO or hybrid it with other atoms on these oxygen-containing functional groups could be a better way to improve rGO performance using in lithium-ion battery.

#### ACKNOWLEDGEMENTS

This work was supported by the national science and technology support program of China (Grant No. 2013BAE04B03), startup fund for advance talent (Grant No. 11-08), education department of Heilongjiang province (Grant No.12521465) and science & technology innovation fund from Harbin administration of science & technology (Grant No. 2012RFLXG032).

#### References

1. J. Su, M. Cao, L. Ren and C. Hu, *J. Phys. Chem. C*, 115 (2011) 14469.
2. J.M. Tarascon and M. Armand, *Nature*, 44 (2001) 359.
3. Z.S. Wu, W.C. Ren, L. Wen, L.B. Gao, Z.P. Chen, G.M. Zhou, F. Li and H.M. Cheng, *ACS Nano*, 4 (2010) 3187.
4. P. Poizot, S. Laruelle, S. Grugeon, L. Dupont and J.M. Tarascon, *Nature*, 407 (2000) 496.
5. C.K. Chan, H.L. Peng, G. Hu, K. McLurath, X.F. Zhang, R.A. Huggins and Y. Cui, *Nat. Nanotechnol.*, 3 (2008) 1587.
6. R. Yazami and P. Touzain, *J. Power Sources*, 9 (1983) 365.
7. K. Nagaura and K. Tozawa, *Prog. Batteries Sol. Cells*, 9 (1990) 209.
8. Ali Abouimra, C. Owen, Compton Khalil Amine and SonBinh T. Ngyen, *J. Phys. Chem. C*, 114 (2010) 12800.
9. H. Yamada, T. Yamato, I. Moriguchi and T. Kudo, *Solid State Ionic.*, 175 (2004) 195.
10. I. Moriguchi, R. Hidaka, H. Yamada, T. Kudo, H. Murakami and N. Nakashima, *Adv. Mater.*, 18

- (2006) 69.
11. H. Yamada, T. Kazuki, M. Komatsu, I. Moriguchi and T. Kudo, *J. Phys. Chem. C*, 111 (2007) 8397.
  12. G. Derrien, J. Hassoun and S.B. Paneros, *Adv. Mater.*, 19 (2007) 2336.
  13. J. Hassoun, G. Derrien, S. Panero and B. Sarosati, *Adv. Mater.*, 20 (2008) 3169.
  14. Y. Yu, L. Gu, C.L. Wang, A. Dhanabalar, P.A.V. Aken and J. Maier, *Angew. Chem. Int. Ed.*, 48 (2009) 6485.
  15. X.W. Lou, C.M. Li and L.A. Archer, *Adv. Mater.*, 21 (2009) 2536.
  16. M.H. Park, K. Kim, J. Kim and J. Cho, *Adv. Mater.*, 22 (2010) 415.
  17. K.S. Noroselo, A.K. Geim, S.V. Morozov, D. Jiang, Y. Zhang, S.V. Dubonos, et al., *Science*, 306 (2004) 666.
  18. D. Chen, G. Ji, Y. Ma, J. Lee and J. Lu, *Appl. Mater. Interfaces*, 3 (2011) 3078.
  19. Y. Zhang, Y.W. Tan, H.L. Stormer and P. Kim, *Nature*, 438 (2005) 201.
  20. H. Wang, L. Cui, Y. Yang, H.S. Casalongue, J.T. Robinson, Y. Liang, Y. Cui and H. Dai, *J. Am. Chem. Soc.*, 132 (2010) 13978.
  21. S. Park and R.S. Ruoff, *Nat. Nanotechnol.*, 4 (2009) 217.
  22. W.S. Hummers and R.E. Offeman, *J. Am. Chem. Soc.*, 80 (1958) 1339.
  23. T. Szabó, A. Szeri and I. Dékány, *Carbon*, 43 (2005) 87.
  24. C. Nethrathathi, J.T. Rajamathi, N. Rarishankar, C. Shivakumare and M. Rajamathi, *Langmuir*, 24 (2008) 8240.
  25. A. Bagri, C. Mattevi, M. Acik, Y. J. Chabal, M. Chhowalla and V. B. Shenoy, *Nat. Chem.*, 2 (2010) 581.
  26. T. J. Davies, R. R. Moore, C. E. Banks and R. G. Compton, *J. Electroanal. Chem.*, 574 (2004) 123.
  27. R.S. Robinson, K. Sternitzke, M.T. McDermott and R.L. McCreery, *J. Electrochem. Soc.*, 138 (1991) 2412.
  28. Z.L. Wang, D. Wu, Y. Huang, Z. Wu, L. Wang and X. Zhang, *Chem. Commun.*, 48 (2012) 976.
  29. X. Tong, H. Wang, G. Wang, L. Wan, Z. Ren and J. Bai, *J. Solid State Chem.*, 184 (2011) 982.
  30. W. Gao, L.B. Alemany, L. Ci and P.M. Ajayan, *Nat. Chem.*, 1 (2009) 403.
  31. Y.Y. Wang, Z.H. Ni, T. Yu, Z.X. Shen and H.M. Wang, *J. Phys. Chem. C*, 112 (2008) 10637.
  32. A.C. Ferrari, J.C. Meyer, V. Scardaci and C. Casiraghi, *Phys. Rev. Lett.*, 97 (2006) 187401.
  33. P. Lian, X. Zhu, S. Liang, Z. Li, W. Yang and H. Wang, *Electrochim. Acta*, 55 (2010) 3909.
  34. E. Strauss, G. Ardel, V. Livshits, L. Burstein, D. Golodnitsky and E. Peled, *J. Power Sources*, 88 (2000) 206.
  35. J.R. Dahn, T. Zheng, Y. Liu and J.S. Xue, *Science*, 270 (1995) 590.
  36. S.B. Yang, H.H. Song and X.H. Chen, *Electrochem. Commun.*, 8 (2006) 137.
  37. J. Giraudet, M. Dubois, J. Inacio and A. Hamwi, *Carbon*, 41 (2003) 453.